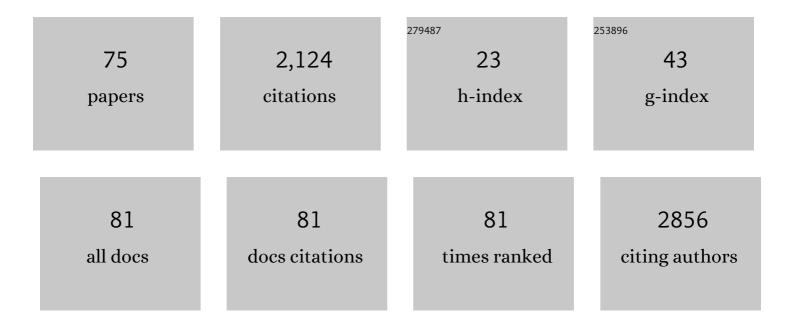
## Tiankai Yao

List of Publications by Year in descending order

Source: https://exaly.com/author-pdf/1595655/publications.pdf Version: 2024-02-01



ΤΙΛΝΚΑΙ ΥΛΟ

#	Article	IF	CITATIONS
1	Highly thermally conductive and mechanically strong graphene fibers. Science, 2015, 349, 1083-1087.	6.0	564
2	Advanced Phase Change Composite by Thermally Annealed Defect-Free Graphene for Thermal Energy Storage. ACS Applied Materials & Interfaces, 2014, 6, 15262-15271.	4.0	113
3	Graphene-based sorbents for iodine-129 capture and sequestration. Carbon, 2015, 90, 1-8.	5.4	91
4	Understanding the mechanical properties of vanadium carbides: Nano-indentation measurement and first-principles calculations. Journal of Alloys and Compounds, 2013, 548, 60-64.	2.8	90
5	Self-accelerated corrosion of nuclear waste forms at material interfaces. Nature Materials, 2020, 19, 310-316.	13.3	61
6	Tunable optical properties and stability of lead free all inorganic perovskites (Cs <sub>2</sub> Snl <sub>x</sub> Cl <sub>6â^'x</sub> ). Journal of Materials Chemistry A, 2018, 6, 2577-2584.	5.2	55
7	Flexible, thorn-like ZnO-multiwalled carbon nanotube hybrid paper for efficient ultraviolet sensing and photocatalyst applications. Nanoscale, 2014, 6, 13630-13636.	2.8	44
8	Bulk Iodoapatite Ceramic Densified by Spark Plasma Sintering with Exceptional Thermal Stability. Journal of the American Ceramic Society, 2014, 97, 2409-2412.	1.9	43
9	Spark plasma sintering (SPS) densified U3Si2 pellets: Microstructure control and enhanced mechanical and oxidation properties. Journal of Alloys and Compounds, 2020, 825, 154022.	2.8	40
10	A universal trend of structural, mechanical and electronic properties in transition metal (M=V, Nb,) Tj ETQq0 0 0	gBT /Over 1.4	logg 10 Tf 50
11	Bubble morphology in U3Si2 implanted by high-energy Xe ions at 300°C. Journal of Nuclear Materials, 2017, 495, 146-153.	1.3	33
19	The influence of lattice defects, recombination, and clustering on thermal transport in single crystal	9.9	20

12	thorium dioxide. APL Materials, 2020, 8, .	2.2	32
13	Structural and relative stabilities, electronic properties and possible reactive routing of osmium and ruthenium borides from first-principles calculations. Dalton Transactions, 2013, 42, 7041.	1.6	31
14	TiO2 doped UO2 fuels sintered by spark plasma sintering. Journal of Nuclear Materials, 2016, 469, 251-261.	1.3	31
15	Nano- and micro-indentation testing of sintered UO2 fuel pellets with controlled microstructure and stoichiometry. Journal of Nuclear Materials, 2019, 516, 169-177.	1.3	30
16	Thermophysical and mechanical property assessment of UB2 and UB4 sintered via spark plasma sintering. Journal of Alloys and Compounds, 2020, 818, 153216.	2.8	29
17	U3Si2 and UO2 composites densified by spark plasma sintering for accident-tolerant fuels. Journal of Nuclear Materials, 2020, 534, 152147.	1.3	29
18	α-U and ω-UZr2 in neutron irradiated U-10Zr annular metallic fuel. Journal of Nuclear Materials, 2020, 542, 152536.	1.3	28

Τιανκαι Υάο

#	Article	IF	CITATIONS
19	Influence of grain growth on the structural properties of the nanocrystalline Gd2Ti2O7. Journal of Nuclear Materials, 2017, 487, 373-379.	1.3	27
20	Grain growth and pore coarsening in dense nanoâ€crystalline UO <sub>2+<i>x</i></sub> fuel pellets. Journal of the American Ceramic Society, 2017, 100, 2651-2658.	1.9	26
21	Radiation-induced grain subdivision and bubble formation in U3Si2 at LWR temperature. Journal of Nuclear Materials, 2018, 498, 169-175.	1.3	25
22	Nano-crystallization induced by high-energy heavy ion irradiation in UO2. Scripta Materialia, 2018, 155, 169-174.	2.6	25
23	Deciphering the degradation mechanism of the lead-free all inorganic perovskite Cs2SnI6. Npj Materials Degradation, 2019, 3, .	2.6	25
24	Combining mesoscale thermal transport and x-ray diffraction measurements to characterize early-stage evolution of irradiation-induced defects in ceramics. Acta Materialia, 2020, 193, 61-70.	3.8	25
25	In situ Investigation of Water Interaction with Lead-Free All Inorganic Perovskite (Cs <sub>2</sub> SnI <i><sub>x</sub></i> Cl <sub>6–<i>x</i></sub> ). Journal of Physical Chemistry C, 2019, 123, 9575-9581.	1.5	23
26	Does the real ReN <sub>2</sub> have the MoS <sub>2</sub> structure?. Physical Chemistry Chemical Physics, 2013, 15, 183-187.	1.3	22
27	Mechanism of iodine release from iodoapatite in aqueous solution. RSC Advances, 2018, 8, 3951-3957.	1.7	22
28	Dense nanocrystalline <scp>UO</scp> <sub>2+<i>x</i></sub> fuel pellets synthesized by high pressure spark plasma sintering. Journal of the American Ceramic Society, 2018, 101, 1105-1115.	1.9	21
29	Structural stability, phase transition, and mechanical and electronic properties of transition metal nitrides MN (M=Tc, Re, Os, and Ir): First-principles calculations. Computational Materials Science, 2012, 56, 116-121.	1.4	20
30	The grain-size effect on thermal conductivity of uranium dioxide. Journal of Applied Physics, 2019, 126,	1.1	20
31	On spinodal-like phase decomposition in U–50Zr alloy. Materialia, 2020, 9, 100592.	1.3	20
32	Facile low temperature solid state synthesis of iodoapatite by high-energy ball milling. RSC Advances, 2014, 4, 38718-38725.	1.7	19
33	Thermally-Conductive andÂMechanically-Robust Graphene Nanoplatelet Reinforced UO2 Composite Nuclear Fuels. Scientific Reports, 2018, 8, 2987.	1.6	19
34	Dense Iodoapatite Ceramics Consolidated by Lowâ€Temperature Spark Plasma Sintering. Journal of the American Ceramic Society, 2015, 98, 3733-3739.	1.9	17
35	Fuel-cladding chemical interaction of a prototype annular U-10Zr fuel with Fe-12Cr ferritic/martensitic HT-9 cladding. Journal of Nuclear Materials, 2021, 544, 152588.	1.3	17
36	In situ synchrotron investigation of grain growth behavior of nano-grained UO2. Scripta Materialia, 2017, 131, 29-32.	2.6	16

Τιανκαι Υάο

#	Article	IF	CITATIONS
37	Chemical Durability and Dissolution Kinetics of Iodoapatite in Aqueous Solutions. ACS Earth and Space Chemistry, 2019, 3, 452-462.	1.2	16
38	Indirect characterization of point defects in proton irradiated ceria. Materialia, 2021, 15, 101019.	1.3	16
39	TEM characterization of dislocation loops in proton irradiated single crystal ThO2. Journal of Nuclear Materials, 2021, 552, 152998.	1.3	16
40	Radiation Stability of Sparkâ€Plasma‣intered Lead Vanadate Iodoapatite. Journal of the American Ceramic Society, 2015, 98, 3361-3366.	1.9	15
41	The thermal stability and consolidation of perovskite variant Cs <sub>2</sub> SnCl <sub>6</sub> using spark plasma sintering. Journal of the American Ceramic Society, 2018, 101, 2060-2065.	1.9	15
42	In-situ TEM study of radiation-induced amorphization and recrystallization of hydroxyapatite. Journal of Nuclear Materials, 2018, 512, 307-313.	1.3	15
43	Out-of-pile and postirradiated examination of lanthanide and lanthanide-palladium interactions for metallic fuel. Journal of Nuclear Materials, 2021, 544, 152727.	1.3	15
44	Understanding spinodal and binodal phase transformations in U-50Zr. Materialia, 2021, 16, 101092.	1.3	14
45	Development of a grain growth model for U3Si2 using experimental data, phase field simulation and molecular dynamics. Journal of Nuclear Materials, 2020, 532, 152069.	1.3	13
46	A systematic study of lanthanide titanates (A2Ti2O7) chemical durability: corrosion mechanisms and control parameters. Corrosion Science, 2021, 185, 109394.	3.0	13
47	Radiation-induced amorphization of Ce-doped Mg2Y8(SiO4)6O2 silicate apatite. Nuclear Instruments & Methods in Physics Research B, 2016, 379, 102-106.	0.6	12
48	Microstructure control of macroscopic graphene paper by electrospray deposition and its effect on thermal and electrical conductivities. Applied Physics Letters, 2017, 110, .	1.5	12
49	In-situ TEM study of the ion irradiation behavior of U3Si2 and U3Si5. Journal of Nuclear Materials, 2018, 511, 56-63.	1.3	12
50	Fabrication and thermophysical properties of UO2-UB2 and UO2-UB4 composites sintered via spark plasma sintering. Journal of Nuclear Materials, 2021, 544, 152690.	1.3	12
51	Understanding fission gas bubble distribution, lanthanide transportation, and thermal conductivity degradation in neutron-irradiated α-U using machine learning. Materials Characterization, 2022, 184, 111657.	1.9	12
52	Fabrication of lanthanum-doped thorium dioxide by high-energy ball milling and spark plasma sintering. Journal of Nuclear Materials, 2017, 485, 207-215.	1.3	11
53	Dislocation loop evolution in Krâ€irradiated ThO <sub>2</sub> . Journal of the American Ceramic Society, 2022, 105, 5419-5435.	1.9	11
54	Correlation between crystallographic orientation and surface faceting in UO2. Journal of Nuclear Materials, 2016, 478, 176-184.	1.3	10

Τιανκαι Υάο

#	Article	IF	CITATIONS
55	Spark plasma sintering-densified vanadinite apatite-based chlorine waste forms with high thermal stability and chlorine confinement. Journal of Nuclear Materials, 2020, 528, 151857.	1.3	10
56	Oxygen point defect accumulation in single-phase <mml:math xmlns:mml="http://www.w3.org/1998/Math/MathML"&gt;<mml:mrow><mml:mi mathvariant="normal"&gt;U<mml:msub><mml:mi mathvariant="normal"&gt;O<mml:mrow><mml:mn>2</mml:mn><mml:mo>+</mml:mo><mml:mi>xPhysical Review Materials, 2019, 3, .</mml:mi></mml:mrow></mml:mi </mml:msub></mml:mi </mml:mrow></mml:math 	0.9 ml:mi> <td>10 1ml:mrow&gt; <!--1</td--></td>	10 1ml:mrow> 1</td
57	Aluminum-doped U3Si2 composite fuels with enhanced oxidation resistance. Journal of Alloys and Compounds, 2021, 853, 157319.	2.8	9
58	In situ monitoring of microstructure evolution during thermal processing of uranium-zirconium alloys using laser-generated ultrasound. Journal of Nuclear Materials, 2021, 553, 153005.	1.3	9
59	Consolidation of commercial-size UO2 fuel pellets using spark plasma sintering and microstructure/microchemical analysis. MRS Communications, 2018, 8, 979-987.	0.8	8
60	Corrosion interactions between stainless steel and lead vanado-iodoapatite nuclear waste form part I. Npj Materials Degradation, 2020, 4, .	2.6	8
61	Radiation-induced amorphization of Langasite La3Ga5SiO14. Journal of Nuclear Materials, 2018, 500, 50-55.	1.3	7
62	Reply to: How much does corrosion of nuclear waste matrices matter. Nature Materials, 2020, 19, 962-963.	13.3	7
63	Corrosion interactions between stainless steel and lead vanado-iodoapatite nuclear waste form part II. Npj Materials Degradation, 2020, 4, .	2.6	7
64	3Y-TZP Toughened and Oxidation-resistant U3Si2 Composites for Accident Tolerant Fuels. Journal of Nuclear Materials, 2021, 544, 152691.	1.3	7
65	Metallization and softening of B6O at high pressure. Journal of Alloys and Compounds, 2014, 600, 71-77.	2.8	6
66	Magnetic, transport and thermal properties of <i>δ</i> -phase UZr <sub>2</sub> . Philosophical Magazine Letters, 2021, 101, 1-11.	0.5	5
67	Lattice strain mapping of cracks and indentations in UO2 using synchrotron microdiffraction. Journal of Nuclear Materials, 2020, 529, 151943.	1.3	4
68	Grain subdivision and structural modifications by high-energy heavy ions in UO2 with different initial grain size. Nuclear Instruments & Methods in Physics Research B, 2022, 515, 48-60.	0.6	4
69	Small-scale mechanical testing and characterization of fuel cladding chemical interaction between HT9 cladding and advanced U-based metallic fuel alloy. Journal of Nuclear Materials, 2022, 566, 153754.	1.3	4
70	Degradation mechanism of lead-vanado-iodoapatite in NaCl solution. Corrosion Science, 2020, 172, 108720.	3.0	3
71	UO2 + 5Â vol% ZrB2 nano composite nuclear fuels with full boron retention and enhanced oxidation resistance. Ceramics International, 2020, 46, 26486-26491.	2.3	2
72	Transmission Electron Microscopy based Characterization of a U-20Pu-10Zr Fuel Irradiated in Experimental Breeder Reactor-II. Journal of Nuclear Materials, 2022, 568, 153846.	1.3	2

#	Article	IF	CITATIONS
73	Enhanced crevice corrosion of stainless steel 316 by degradation of Cr-containing hollandite crevice former. Corrosion Science, 2022, 205, 110462.	3.0	2

First-principles study of structural stability, elastic and electronic properties of ternary rare earth-transition metal—Borides and carbides (RTxZ, R=Sc, Y, and La, T=Pt and Pd, Z=B and C, and x=2, 3,) Tj ETQq**Q.®** O rgBT1/Overlock